PHYSICAL REVIEW D **110,** 124063 (2024)

Stability of hypermassive neutron stars with realistic rotation and entropy profiles

Nishad Muhammed,[1,*] Matthew D. Duez,[1,†] Pavan Chawhan,[1] Noora Ghadiri,[2] Luisa T. Buchman,[1]
Francois Foucart,[3] Patrick Chi-Kit Cheong,[3,4] Lawrence E. Kidder,[5] Harald P. Pfeiffer,[6] and Mark A. Scheel[7]
[1]*Department of Physics and Astronomy, Washington State University, Pullman, Washington 99164, USA*
[2]*Department of Physics, University of Illinois at Urbana-Champaign, Urbana, Illinois 61801, USA*
[3]*Department of Physics and Astronomy, University of New Hampshire,*
9 Library Way, Durham, New Hampshire 03824, USA
[4]*Department of Physics, University of California, Berkeley, Berkeley, California 94720, USA*
[5]*Cornell Center for Astrophysics and Planetary Science, Cornell University, Ithaca, New York 14853, USA*
[6]*Max Planck Institute for Gravitational Physics (Albert Einstein Institute),*
Am Mühlenberg 1, D-14476 Potsdam, Germany
[7]*TAPIR, Walter Burke Institute for Theoretical Physics, MC 350-17, California Institute of Technology,*
Pasadena, California 91125, USA

(Received 21 May 2024; accepted 20 September 2024; published 26 December 2024)

Binary neutron star mergers produce massive, hot, rapidly differentially rotating neutron star remnants; electromagnetic and gravitational wave signals associated with the subsequent evolution depend on the stability of these remnants. Stability of relativistic stars has previously been studied for uniform rotation and for a class of differential rotation with monotonic angular velocity profiles. Stability of those equilibria to axisymmetric perturbations was found to respect a turning point criterion: along a constant angular momentum sequence, the onset of unstable stars is found at maximum density less than but close to the density of maximum mass. In this paper, we test this turning point criterion for nonmonotonic angular velocity profiles and nonisentropic entropy profiles, both chosen to more realistically model postmerger equilibria. Stability is assessed by evolving perturbed equilibria in 2D using the Spectral Einstein Code. We present tests of the code's new capability for axisymmetric metric evolution. We confirm the turning point theorem and determine the region of our rotation law parameter space that provides highest maximum mass for a given angular momentum.

DOI: 10.1103/PhysRevD.110.124063

I. INTRODUCTION

Binary neutron star mergers are important multimessenger astrophysical sources and probes of high-density matter. Gravitational waves from the late inspirals of such events have now been detected [1,2], in one case accompanied by electromagnetic counterparts [3]. The high-frequency postmerger gravitational waveform and the electromagnetic signals (e.g., kilonova, gamma ray burst) are sensitive to the fate of the postmerger remnant. This will be a hot, rapidly and differentially rotating star, which, depending on the binary mass and the equation of state, might collapse promptly to a black hole, might persist until secular evolution drives it to an unstable state followed by collapse, or might persist for longer times as a supramassive neutron star or indefinitely as a regular neutron star. In delayed and no collapse cases, the remnant persists for many dynamical timescales, therefore in quasiequilibrium configurations. The presence and timescale of prompt or delayed collapse depends crucially on the stability of these equilibria to collapse. (For review of binary neutron stars, see [4–6].)

Although the stability of stellar equilibria is a classic problem [7–12], the stability of hypermassive neutron stars is addressed in relatively few studies (e.g., [13–16]), and much remains unknown. Stability of relativistic stellar equilibria can be determined by finding the eigenfrequencies of linear perturbations or by full nonlinear numerical evolutions. A way of evaluating stability from equilibria alone, without any sort of evolution, would be extremely helpful. This explains interest in turning point methods, which provide information about stability from sequences of equilibria. A sequence here means a one-dimensional slice in the space of equilibria, usually parametrized by the maximum baryonic density $\rho_{\max}$. For arbitrary rotation, entropy, and composition profiles, this space would be infinite dimensional.

The turning point theorem [11,12,17] applies to uniformly rotating stars. It assumes a one-parameter equation of state and, furthermore, that the pulsations of the star are

---

[*] Contact author: nishad.muhammed@wsu.edu
[†] Contact author: m.duez@wsu.edu

governed by the same one-parameter equation of state. Because uniform rotation is presumed to persist, it is a criterion for secular stability, i.e., stability on timescales on which uniform rotation is enforced. The theorem applies to axisymmetric modes, the ones related to collapse, and does not address nonaxisymmetric rotational instabilities. [Indeed, many quasitoroidal differentially rotating neutron stars are found to be unstable to nonaxisymmetric (one-arm and bar mode) instabilities [16].] The space of equilibria is then two-dimensional, with total baryonic mass M_0 (the number of nucleons multiplied by a fiducial mass per baryon) and total angular momentum J uniquely determining a star. A constant-J subspace is a 1D sequence. If the total gravitational mass M on the sequence has a maximum, then stars on the sequence at higher $\rho_{\max}$ are unstable. The neutral point on the sequence separating secularly stable from unstable stars is at slightly lower $\rho_{\max}$ for nonzero J [17]. Numerical evolutions find the dynamical stability neutral point to be close to the turning point [13,18].

The turning point theorem does not apply to differentially rotating or nonisentropic stars, but Kaplan *et al.* [19] conjecture that the turning point criterion remains approximately valid. Their argument presumes that equilibrium M depends to first order only on conserved quantities M_0, J, and total entropy S, and not on the angular momentum and entropy distributions. They also note that only "approximate turning points" (not all conserved quantities having extrema at the same point on the sequence) are found in general, but they propose that this will be sufficient.

The stability of hypermassive neutron stars was studied, and the conjecture by Kaplan *et al.* tested, by Weih *et al.* [13] using numerical evolutions of these equilibria. To construct equilibria, one must choose a rotation profile, and Weih *et al.* chose the j-constant law,

$$j(\Omega) = A^2(\Omega_c - \Omega), \tag{1}$$

where j is the specific angular momentum, Ω is the angular velocity, Ω_c is the central angular velocity, and A is a free parameter with dimensions of length which controls the degree of the differential rotation. The name j-constant is chosen because in the Newtonian limit the specific angular momentum is constant [20,21].

Rotation profiles constructed with this law have Ω that monotonically decreases with distance from the center of the star. As Weih *et al.* themselves note, this is not a good match for the rotation profiles observed in remnants produced by binary neutron star merger simulations, which predict a nonmonotonic Ω that peaks some distance away from the rotation axis [22–28]. Rotation laws that do capture this $\Omega(r)$ profile shape have been constructed by Uryū *et al.* [29]. The key idea is to specify Ω as a function of j rather than vice versa. In particular, one such profile is

$$\Omega(j;\Omega_c) = \Omega_c \frac{1 + [j/(B^2\Omega_c)]^p}{1 + [j/(A^2\Omega_c)]^{q+p}}, \tag{2}$$

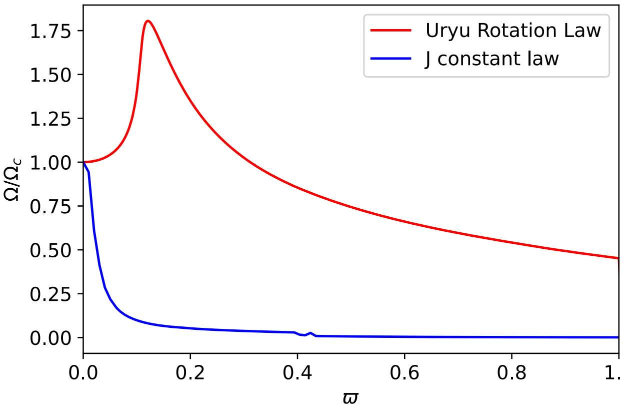

FIG. 1. Angular velocity Ω normalized to Ω_c as a function of coordinate distance from the axis ϖ along the equator for two rotation laws. The top curve uses Eq. (2) with $p = 1$, $q = 3$, $A = 0.96$, $B = 0.73$. The bottom curve uses Eq. (1) with $A = 0.2$.

where A, B, q, and p are specified constants. An example of rotation profiles produced with the two laws is shown in Fig. 1.

In this paper, which may be considered an extension of the study of Weih *et al.*, we investigate the stability of hypermassive stars with nonmonotonic angular velocity profiles. Furthermore, we consider a range of (convectively stable) entropy profiles within the range plausible for binary neutron star mergers. We introduce a new 2D axisymmetric implementation of the Spectral Einstein Code for our numerical evolutions. Our results vindicate the approximate turning point criterion. In addition, we survey the parameter space of Uryū *et al.* type rotation laws, seeing which values of the parameters are conducive to high maximum mass.

The organization of the paper is as follows. In Sec. II, we discuss the methods of building our initial data and carrying out evolutions. Next, in Sec. III, we discuss the numerical experiments undertaken for this study. Results are presented and analyzed in Sec. IV. We summarize and conclude in Sec. V. We use the geometrized units, in which $c = G = M_\odot = 1$, unless stated otherwise.

II. EQUILIBRIA AND EVOLUTION METHODS

A. Equation of state and entropy profile

The matter in the star is modeled as a perfect fluid with stress-energy tensor,

$$T^{\mu\nu} = \rho h u^\mu u^\nu + P g^{\mu\nu}, \tag{3}$$

where ρ is the baryonic density, h is the specific enthalpy, u^μ is the 4-velocity, and P is the pressure. The neutron star matter is modeled using the DD2 equation of state [30]. DD2 provides P and h as functions of baryonic density ρ, temperature T, and reduced electron fraction Y_e. It is based on a relativistic mean field model and is publicly available in tabulated form at [31,32]. It predicts radius $R_{\mathrm{NS}} = 13.1$ km and tidal deformability $\Lambda = 860$ for a $1.35 M_{\odot}$ neutron star.

Our algorithm for constructing equilibrium models requires one-dimensional equations of state (EOS); $P = P_{\mathrm{eq}}(\rho)$. The 1D EOS we use for equilibrium construction are one-dimensional cuts of DD2, created by imposing two conditions to determine Y_e and T for each ρ. The first condition is beta equilibrium; $\mu_p + \mu_e = \mu_n + \mu_\nu$, where we take the electron neutrino chemical potential μ_ν to be zero. The second condition is an explicit choice for the dependence of specific entropy s on density; $s = s_{\mathrm{eq}}(\rho)$. We also produce one EOS, `ColdStar`, for which the temperature is $T = 0.01$ MeV, the table minimum temperature. Based on the choice of $s_{\mathrm{eq}}(\rho)$, we have the following nomenclature for the EOSs; `CE1` corresponds to constant specific entropy, $s = 1\ \mathrm{k}_B/\mathrm{baryon}$, `CE2` corresponds to $s = 2.2\ \mathrm{k}_B/\mathrm{baryon}$. `VE1` is a variable entropy cut motivated by the thermodynamic profile of the merger remnant in Perego *et al.* [33]. It has specific entropy varying between 10^{-3}–$6\ \mathrm{k}_B/\mathrm{baryon}$ for NS density range 10^{12}–$10^{16}\ \mathrm{gm/cm^3}$. `VE2` has entropy varying between $3\ \mathrm{k}_B/\mathrm{baryon}$ and $1\ \mathrm{k}_B/\mathrm{baryon}$ for the same density range.

Profiles of EOS cuts are shown in Fig. 2, where we plot more than three decades of density up to the highest neutron star maximum density, the range relevant to the structure of our stars. Comparison of P to $P_c(T = 0.01\ \mathrm{MeV})$ indicates the degree of degeneracy; we see that the cores are always degenerate but the envelopes are not (reflecting the expected outcome of mergers). Because of entropy and composition (Y_e) gradients in the equilibrium star, when perturbed, these stars will move to regions of the equation of state space outside the cut used to construct equilibria, another way in which our stars fall outside the domain of turning point theorems. Therefore, we also compare $\Gamma \equiv d \ln P / d \ln \rho|_{s=s_{\mathrm{eq}}(\rho)}$ to $\Gamma_{\mathrm{ad}} \equiv d \ln P / d \ln \rho|_{\mathrm{s=const}}$ to indicate the strength of buoyancy forces in the nonisentropic cases.

The entropy profile for `VE1` has a sharp change in slope, which leads to a density regime of very shallow P vs ρ. In fact, $dP/d\rho$ is actually slightly negative in the range $2 \times 10^{14}\ \mathrm{gm/cm^3}$–$2.5 \times 10^{14}\ \mathrm{gm/cm^3}$, which can be seen in the plot of Γ. (Note that this is neither an isothermal nor an adiabatic derivative; the fluid is thermodynamically stable, and sound waves are stable.) In practice, the equilibrium solve “jumps over” this density region, so $P(\rho)$ is effectively flat, reminiscent of a first-order phase transition, and the resulting stellar profiles have an abrupt jump in density. Although inadvertent, this feature allows us to test the turning point criterion for equilibria with density jumps, a feature which might appear in postmerger remnants if a first-order phase transition from hadronic to quark matter is present [34–38].

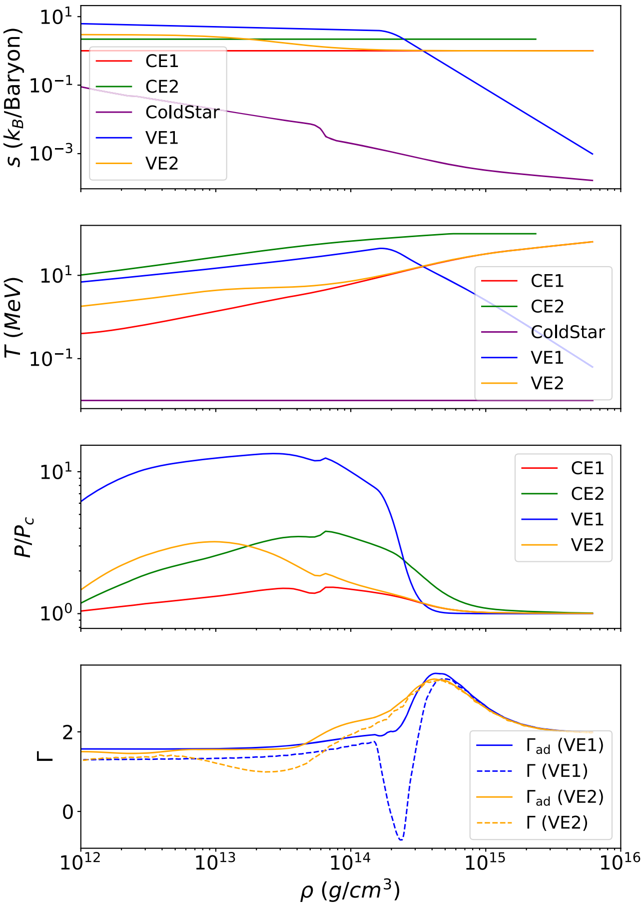

FIG. 2. Profiles of different EOS cuts plotted for density range 10^{12}–$10^{16}\ \mathrm{gm/cm^3}$. *First panel*: specific entropy against density. *Second panel*: temperature against density. *Third panel*: P/P_c against density, where P_c is the pressure corresponding to `ColdStar`. *Fourth panel*: Γ against density.

B. Rotation profile and construction of equilibria

We produce axisymmetric equilibrium configurations using the code of Cook *et al.* [39,40], which we call “RotNS.”

The spacetime metric is written in the form

$$ds^2 = -e^{\gamma+\lambda} dt^2 + e^{2\alpha}(dr^2 + r^2 d\theta^2) + e^{\gamma-\lambda} r^2 \sin^2\theta (d\phi - \omega dt)^2. \tag{4}$$

The fluid motion is taken to be azimuthal, so the proper velocity v, the Lorentz factor u^t, and the specific angular momentum j are

$$v = (\Omega - \omega) r \sin\theta e^{-\lambda}, \tag{5}$$

$$u^t = (1 - v^2)^{-1/2} e^{-(\rho+\gamma)/2}, \tag{6}$$

$$j \equiv u^t u_\phi = (u^t)^2 e^{\gamma-\lambda} r^2 \sin^2\theta (\Omega - \omega). \tag{7}$$

An integrability condition on the equation of hydrostatic equilibrium requires we choose for the rotation law either uniform rotation ($\Omega = \text{constant}$) or that $j = j(\Omega)$ or $\Omega = \Omega(j)$. The original RotNS used the law $j(\Omega) = A^2(\Omega_c - \Omega)$ for constant A. This law does not allow nonmonotonic rotation profiles of the sort seen in binary neutron star simulations. Such profiles can be constructed if j is taken to be the independent variable. Thus, following Uryū *et al.* [41], we implement the following rotation law:

$$\Omega(j;\Omega_c) = \Omega_c \frac{1 + j/(B^2\Omega_c)}{1 + [j/(A^2\Omega_c)]^4}, \tag{8}$$

i.e., we choose $p = 1$, $q = 3$ from the more general law, Eq. (2). A typical profile is shown in Fig. 1.

Given Ω_c, one can find j at any point (r,θ) by finding the root of $f_j(j) \equiv u^t(\Omega[j])u_\phi(\Omega[j]) - j = 0$. Given j at each point, the matter distribution is given by the Bernoulli integral,

$$\begin{aligned} H(\rho) &= H_{\rm eq}(j;\Omega_c) \\ &= \frac{1-\zeta}{\sqrt{1-v^2}} \exp[-(\lambda+\gamma)/2 + I(j;\Omega_c)], \end{aligned} \tag{9}$$

where H is the nonisentropic generalization of the specific enthalpy [42],

$$\ln(H) \equiv \int_0^P \frac{dP}{\rho h}. \tag{10}$$

Here the integral is taken along the curve $s = s_{\rm eq}(\rho)$, ζ is an integration constant, and the rotation profile integral

$$I(j;\Omega_c) = \int_0^j j' \frac{d}{dj'}\Omega(j';\Omega_c)dj', \tag{11}$$

is messy but analytic.

Let us call the equatorial radius r_e, the polar radius r_p, the maximum density $\rho_{\rm max}$ and its coordinate distance from the axis r_m. To find a model for a single equilibrium, RotNS specifies $\rho_{\rm max}$ and the ratio $\hat{r}_p \equiv r_p/r_e$. In addition to solving for the metric, one needs to determine the appropriate constants Ω_c and ζ. This is done by an iterative process of refining an initial guess. For the first $\rho_{\rm max}$ of each sequence, we start with a TOV star and then adjust $\hat{r}_p$ downward until the angular momentum J reaches the desired value $J_{\rm seq}$, a 1D root find for $J(\hat{r}_p) - J_{\rm seq}$. For the next $\rho_{\rm max}$, the star on the sequence for the previous $\rho_{\rm max}$ serves as the initial guess.

The procedure for determining the global constants is the following straightforward generalization of the original RotNS. First, we define scaled metric potentials $\hat{\rho} \equiv \rho r_e^{-2}$, $\hat{\gamma} \equiv \gamma r_e^{-2}$, $\hat{\alpha} \equiv \alpha r_e^{-2}$. These shall be taken as fixed for the relaxation procedure.

At the pole, $\Omega = \Omega_c$, $v = j = 0$, $h = 1$, so

$$\begin{aligned} 1 &= H_{\rm eq}(j=0, r=0;\Omega_c) \\ &= (1-\zeta)e^{(\rho_p+\gamma_p)/2 + I(0;\Omega_c)}, \end{aligned} \tag{12}$$

which provides an equation for ζ. There are also two equations at the equator ($r = r_e$, $\theta = \pi/2$, $j = j_e$) and another two at the point of maximum density ($r = r_m$, $\theta = \pi/2$, $j = j_m$). These equations are

$$1 = H_{\rm eq}(j = j_e, r = r_e, \theta = \pi/2; \Omega_c), \tag{13}$$

$$j_e = [u^t u_\phi](j = j_e, r = r_e, \theta = \pi/2; \Omega_c), \tag{14}$$

$$H(\rho_{\rm max}) = H_{\rm eq}(j = j_m, r = r_m, \theta = \pi/2; \Omega_c), \tag{15}$$

$$j_m = [u^t u_\phi](j = j_m, r = r_m, \theta = \pi/2; \Omega_c). \tag{16}$$

We solve these using Newton's method for the global parameters (Ω_c, j_m, j_e, r_e). When the maximum density is at the center, we use instead a 2D root finder, solving Eqs. (13) and (14) for (Ω_c,j_e).

The parameters A and B in Eq. (8) must also be specified. In some sequences below, we take them to be constant. Alternatively, we can fix the ratios $\Omega_{\rm max}/\Omega_c$ and Ω_e/Ω_c, where $\Omega_{\rm max}$ is the maximum value of Ω (note: not the value of Ω where $\rho = \rho_{\rm max}$), and Ω_e is the equatorial Ω. Given these ratios, A and B can be determined by a 2D root find, which does not converge for desired angular momentum if the solve for A and B is performed within the relaxation for a single model. Instead, the solver for A and B must be the outer stage of the relaxation. If precise values of the ratios are not needed, a close approximation is obtained by solving for A and B at the completion of each successful new model, assuming one takes fairly small steps in $\rho_{\rm max}$. Fixing angular velocity ratios is what was used for the sequences in Uryū *et al.* [41].

We stress that there is no correct or (known) physically realistic choice in how to specify A and B. This is part of the ambiguity inherent in defining sequences and attempting to apply a turning point criterion in a parameter space of differentially rotating stars, something that is less likely to be noticed when using a rotation law family (like the j-constant family) with only one differential rotation parameter, which might seem natural to hold constant. Whether this ambiguity turns out to be important in predicting stability is something we address in this study.

C. Numerical evolution

We evolve using the Spectral Einstein Code (SpEC) [43]. SpEC evolves the fluid using a conventional high-resolution shock capturing finite difference method, and it evolves the spacetime metric in the generalized harmonic formulation using a multidomain pseudospectral method.

Because the unstable mode triggering radial collapse is expected to be axisymmetric, and because we evolve many equilibria, we use the 2D axisymmetric version of SpEC. Our multipatch 2D hydrodynamics code is described in detail in Jesse *et al.* [44]. In that work, we had not developed an axisymmetric version of the pseudospectral metric evolution, so we were forced to evolve the metric on a 3D grid of colocation points for those applications with dynamical spacetimes. Although inefficient, this method allowed accurate simulations of differentially rotating neutron stars for tens of milliseconds, but eventually such simulations succumbed to accumulating growth of violations in the constraint equations.

Here we introduce a new fully 2D version of SpEC, with metric evolution now carried out on a 2D grid representing a meridional cut through the presumed axisymmetric system. Derivatives in the spatial direction perpendicular to the evolution plane are computed using the Cartoon method [45,46]. The Cartoon method solves the symmetry condition for tensor T; $\mathcal{L}_{\partial/\partial\phi}T = 0$. (As Hilditch *et al.* [46] explain, this technique can be applied essentially unchanged even for spatial derivatives of the metric $\partial_k g_{\alpha\beta}$ even though this is not a covariant tensor.)

Given axisymmetry, only one side of the axis on a 2D cut needs to be evolved; the other is determined by the symmetry and can be replaced by appropriate symmetry/regularity boundary conditions on the axis. For this project, we have taken the algorithmically simpler path of evolving both sides. The spectral grid is then constructed of concentric circular wedge domains (corresponding to Chebyshev radial basis functions and Fourier angular basis functions) with a filled shape in the center (corresponding to Matsushima-Marcus basis functions [47]). We choose angular colocation points such that no points lie on the axis, and the grid is exactly symmetric across the axis.

In principle, roundoff error could lead to a breakdown of the symmetry across the axis. This does not appear to be an issue in our simulations, but we have carried out simulations which enforce symmetry by replacing each component $g_{\mu\nu}$ and $\partial_\alpha g_{\mu\nu}$ after each time step with the average of the component on both sides of the axis (with appropriate symmetry factors). This is inexpensive because symmetric pairs of points lie on the same domain and thus on the same processor. We see little difference with or without averaging but have used it for the simulations reported here.

Filtering is necessary for long-term stable evolutions, and it is applied to the spacetime evolution variables, i.e., the 4-metric and its evolved first spacetime derivatives. In each subdomain of the pseudospectral grid, there will be two natural internal coordinates; Cartesian-like for rectangular domains, polarlike for circular annuli. For internal coordinate d, spectral expansion of functions are carried out using basis functions $P_i(x_d)$, where the mode number i is between 0 and N_d. Filtering is done by suppressing basis function expansion coefficients for high-i modes. In angular directions, we always set the highest two modes to zero. In all directions, we multiply the expansion coefficients by a suppression factor of the form $\exp[-\alpha(i/N_d)^P]$, where a wide range of α and P choices are acceptable, so long as they are chosen to affect only the highest modes but to suppress them strongly.

Figures 3 and 4 show the results of some tests of the new code. First, we perform a very long-time evolution of a Kerr-Schild black hole with spin $a/M = 0.5$. The system should be stationary but involves strong curvature. The grid consists of 17 concentric annuli covering radii $1.82M$–$800M$ with total number of radial and angular gridpoints (N_r, N_ϕ) of (306, 18), (374, 22), and (442, 26) at resolutions Lev1, Lev2, and Lev3, respectively. Results are shown in Fig. 3. On the top panel, we plot the violation of the generalized harmonic constraints C, normalized to the size of the terms in the constraints N_C. For each, we compute a volume integral L_2 norm; $L_2(u) \equiv \sqrt{(\int u^2 dV)/(\int dV)}$. Constraint plots see rapid convergence with resolution and a quick settling to numerical equilibrium followed by stasis through the end of

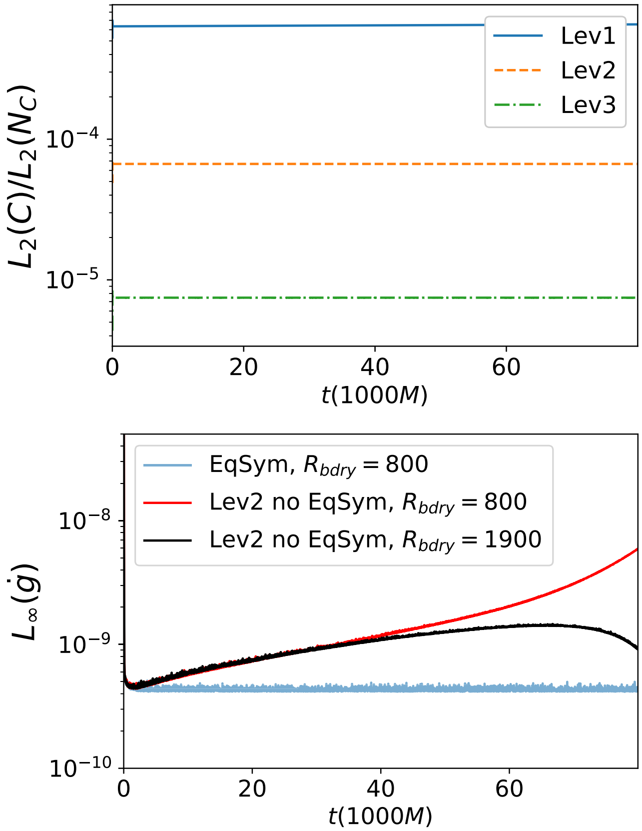

FIG. 3. Test evolutions of an isolated Kerr black hole in 2D. *Top*: the constraint violation at three resolutions. *Bottom*: the norm on the time derivative of the metric. Runs all have the same resolution, corresponding to Lev2. They differ in whether equatorial symmetry ("EqSym") is imposed and in the location of the outer boundary $R_{\rm bdry}$.

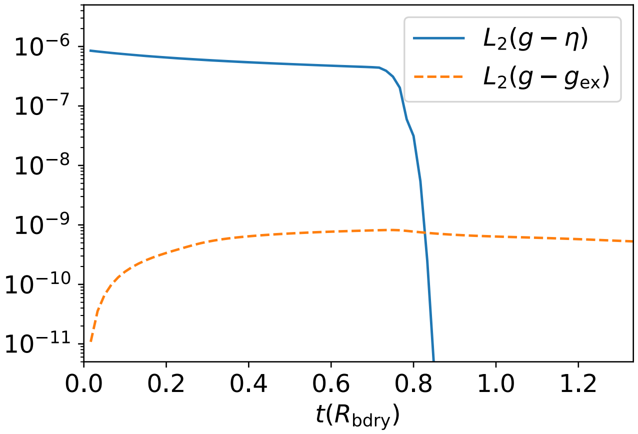

FIG. 4. Tests of SpEC's 2D metric evolution code. Error for an axisymmetric gravitational wave. The sharp drop in $L2(g-\eta)$ (the deviation of the metric from Minkowski) is when the wave reaches the outer boundary at $r = R_{\rm bdry}$ and passes through.

the evolution at $80{,}000M$. For these tests, we impose not only symmetry across the symmetry axis, but also symmetry across the equator. The reason for this is to counteract a issue with the gauge boundary condition in the SpEC code, previously reported in binary black hole simulations [48,49], which causes the center of mass to drift at late times if symmetries are not explicitly imposed. The radial and angular filtering mentioned above is also crucial for good late-time behavior in this test. A demonstration of the gauge effect is shown in the bottom panel, which includes for comparison two runs which did not impose equatorial symmetry. Here we plot the L_∞ norm of $\sqrt{\Sigma_{\alpha\beta}\partial_t g^2_{\alpha\beta}}$, where the time derivative is computed from the difference in the metric over time interval $\Delta t = M$. This norm is much more sensitive to subtle dynamics than the constraint violations and shows the onset of trouble, when present, much sooner. All runs in this plot have Lev2 resolution, but some have extra annuli to extend the outer boundary to $1{,}900M$. We see that failing to impose equatorial symmetry leads to a drift in the metric, although it is ameliorated by moving the outer boundary farther away.[1]

For a dynamical vacuum problem, we evolve a radially outgoing $\ell = 2$, $m = 0$ gravitational wave packet. The packet initial amplitude is a Gaussian with width 1.5 and peak amplitude $10^{-4.5}$ centered at distance $r = 15$ from the origin. The outer boundary for the run shown in the figure is at $R_{\rm bdry} = 60$. For the reported simulation, the total grid $(N_r, N_\phi) = (468, 22)$ (including the circle in the middle). The wave propagates to the boundary and leaves the grid, with $g_{\alpha\beta}$ remaining very close to the analytic solution of the linearized Einstein equations. We demonstrate this by comparing $L_2(g_{\alpha\beta} - g^{\rm lin}_{\alpha\beta})$ (our error, plus the small effect of nonlinearities) to $L_2(g^{\rm lin}_{\alpha\beta} - \eta_{\alpha\beta})$ (a measure of the strength of the wave). Eventually, after about 36 $R_{\rm bdry}$, long after the wave has passed, constraint violations begin to grow and eventually spoil the simulation. This is another manifestation of the boundary problem, and it can be delayed—apparently without limit—by moving the outer boundary sufficiently outward. One might find it surprising that this particular simulation evolved low-amplitude, residual scattered gravitational waves on Minkowski space for less time than the black hole simulation was able to evolve a strongly curved spacetime, but that is only because the boundary was so much closer in the wave test.

Both of these tests indicate a need to improve the outer boundary condition in 2D simulations for future studies involving very long evolution times. Checks of our ability to accurately and stably evolve equilibrium rotating star spacetimes are reported in the next section.

III. SEQUENCES AND STABILITY TESTING

For this study, we have evolved more than 200 models on 31 different constant angular momentum sequences. The initial data for these models are characterized by different angular momenta, four different 1D EOS (encompassing nonisentropic variants) and two distinct rotation laws. The angular momenta, EOS details, parameters of Uryū rotation

TABLE I. List of constant-J sequences in this study. From left to right, the columns represent the entropy profiles, angular momenta, Uryū rotation law parameters A, B, and sequence names, respectively.

EOS	J	A	B	Name	Δ
CE1	6	0.79	0.55	A	0.041 ± 0.024
	6.5	0.79	0.55	B	0.063 ± 0.009
	8.5	1.45	1.48	C	0.059 ± 0.014
	11	1.61	1.64	D	0.099 ± 0.006
	10	1.22	0.92	E	0.108 ± 0.020
	11	1.10	0.83	F	0.101 ± 0.014
CE2	11	0.96	0.73	G	0.095 ± 0.018
	10	0.87	0.60	H	0.099 ± 0.014
	10	0.91	0.63	I	0.096 ± 0.010
	10	0.82	0.57	J	0.072 ± 0.014
	11	0.89	0.62	K	0.061 ± 0.008
	11	0.94	0.65	L	0.096 ± 0.010
	9	0.88	0.60	M	0.066 ± 0.021
	9	1.03	0.72	N	0.089 ± 0.012
VE1	10	0.65	0.45	O	0.100 ± 0.005
	7	0.65	0.45	P	0.096 ± 0.096
	4	0.65	0.45	Q	0.075 ± 0.003
VE2	10	1.08	0.75	R	0.083 ± 0.005
	7	0.98	0.68	S	0.080 ± 0.009
	7	1.08	0.75	T	0.063 ± 0.009
	4	0.93	0.65	U	0.068 ± 0.007

---

[1] An earlier version of this paper on arXiv reports this drift as an always-present, unsolved problem. This was before we tried imposing equatorial symmetry and slightly stronger filtering.

law (A, B), and names of these sequences are reported in Table I. Also included for each sequence is the number Δ which quantifies the difference between the density of maximum mass ($\rho_{\max}$) and the critical density separating stable from unstable configurations ($\rho_{\rm crit}$). We define $\Delta = (\rho_{\max} - \rho_{\rm crit})/\rho_{\max}$. Because only a discrete set of equilibria are evolved, we actually only know the density of the highest-density stable evolved model, $\rho_{\rm stable}$, and of the lowest-density unstable evolved model, $\rho_{\rm unstable}$. Thus, we estimate $\rho_{\rm crit} = (\rho_{\rm stable} + \rho_{\rm unstable})/2$ and calculate the associated error as $(\rho_{\rm unstable} - \rho_{\rm stable})/(2\rho_{\max})$. For the ease of visibility, we have not shown all the models we evolved on the plots to avoid too many data points on the sequences. The stability tests are conducted on a dynamical timescale spanning a few oscillation periods. This is adequate for assessing stability, as the collapse of a dynamically unstable hypermassive neutron star into a black hole occurs within this timescale. As a result, no viscous or radiation effects are included.

The fluid is evolved on a 2D uniform Cartesian grid, covering a square that includes the star. The metric is evolved on a separate 2D pseudospectral grid. The pseudospectral grid includes a disk at the center surrounded by concentric annuli. The disk and the annuli all have the same angular resolution. The outer annuli are chosen to have larger radial extent than the inner ones to allow grid to be concentrated inside the star.

We carry out tests on unperturbed models to determine adequate grid resolution. Six different resolutions for the fluid and pseudospectral grid are used, labeled "Lev1" through "Lev6," with Lev1 the lowest and Lev6 the highest resolution. It should be noted that these resolutions are distinct from the resolutions for 2D dynamical metric evolution discussed in Sec. II.

Figure 5 demonstrates the effect of resolution on evolution. We plot maximum density and the L_2-norm of generalized harmonic constraint $[L_2(C)/L_2(N_c)]$ against time. We see convergence toward stationarity and constraint satisfaction at low resolutions, but at sufficiently high resolution, deviation from equilibrium and constraint violation are dominated by the finite error of the RotNS initial data. As is evident from the figure, increasing the resolution beyond Lev3 does not have a significant impact on maximum density and $L_2(C)/L_2(N_c)$. The resolution of the Lev3 fluid grid is 300^2 colocation points extending up to ~18 km. Its pseudospectral grid has a disk at the center followed by five concentric annuli with angular extents of 50 for all of them. The total number of radial layers of colocation points (unevenly spaced, as mentioned above) is 564, extending out to a distance of 2940 km.

When testing stability, it is useful to introduce a perturbation in the equilibrium configuration, rather than relying on truncation error to produce a resolution-dependent perturbation. As our perturbation, we slightly increase the conserved energy evolution variable τ [44] in the envelope, corresponding to a small increase in the temperature and hence the pressure of the outer layers. This reduces the pressure gradient countering gravity and so leads to a small contraction of the core. We check that the perturbation is small enough that the initial violation of the constraint equations is not increased. Furthermore, we ensure that varying the amplitude of the perturbation does not alter which stars are stable and which are unstable for a sample sequence.

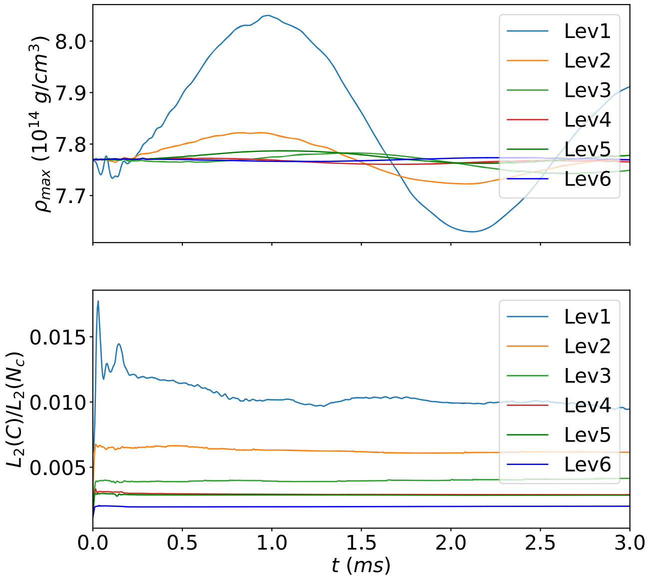

FIG. 5. Convergence tests for a sample hypermassive star with a maximum energy density of 8.897×10^{14} g/cm^3 from sequence F (see Table I). Lev1 through Lev6 represent low to high resolution, respectively. The optimal grid resolution found was Lev3. *Top*: maximum baryonic density vs time; *Bottom*: normalized error of the generalized harmonic constraints.

Figure 6 illustrates the rotation profile of sequence G at $t = 0$ ms and at $t = 6$ ms (at the end of the dynamical evolution). Note that the Ω does not monotonically decrease with radius but has a peak between the center and the equator. Since we are simulating postmerger remnantlike stars, we use $\Omega_{\max}/\Omega_c$ in the range 1.4–2.1 and $\Omega_{\rm eq}/\Omega_c$ in the range 0.3–0.8 for our evolutions [24].

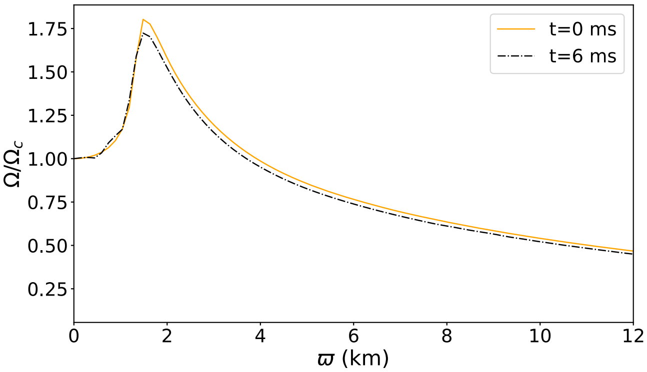

FIG. 6. Angular velocity Ω as a function of coordinate distance from the rotation axis ϖ along the equator at $t = 0$ ms and $t = 6$ ms with A = 0.96 and B = 0.73.

The rotation profile is preserved throughout the evolution, indicating the model is in equilibrium. This is in contrast to what was found for some toroidal stars with this rotational profile evolved under the assumption of conformal flatness [50]. The figure shows Ω of a model with $\rho_{\max} = 7.3 \times 10^{15}\ \mathrm{g\,cm^{-3}}$. We checked Ω for higher-energy density stable stars on the sequence, and they show the same stationarity. Furthermore, the density profile also does not change much (less than 4% at all points on the axis).

IV. RESULTS

A. Stability

In this subsection, we discuss the main results regarding stability. Figure 7 displays the evolution of the models on one of the equilibrium sequences (sequence G). Here we show some representative models that were evolved for this sequence near the turning point. The maximum density normalized to its initial value against time is presented. The evolution was performed for 6 ms. The perturbation was applied on the stars at $t = 0$. Notice that the stars with the higher energy densities collapse within the dynamical timescale (∼1–2 ms). The low-energy density stars, on the other hand, oscillate about their equilibria but remain stable on the relevant timescale. All the stars that are stable fall on the low density side of the turning point (for this particular sequence at $\sim 0.97 \times 10^{15}\ \mathrm{g/cm^3}$), thus obeying the turning point criterion. This feature can be observed in all the other sequences, where the higher-energy density stars will collapse within ∼1–2 ms and the lower density stars are stable and oscillate. All the stars on the left side of the turning point are not necessarily stable as pointed out by Weih *et al.* [13]. Since the actual onset of instability is marked by the neutral stability point which may lie to the left of the turning point [17], some stars on the left side of the turning point are unstable. Nevertheless, it can still be concluded that the instability is reached at or before the turning point, making the turning point criterion a sufficient condition for instability. Our findings for all the sequences conform to this. The oscillations in the stable stars are due to the perturbation. If the same star is evolved without perturbation, the oscillation amplitude is much smaller (although not exactly zero, due to truncation error).

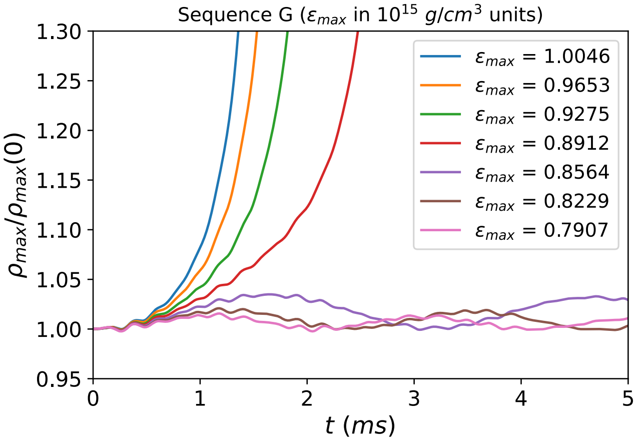

FIG. 7. Evolution of the maximum baryonic density normalized to its initial value. All models are from the same sequence G with $A = 0.96$ and $B = 0.73$. The labels indicate the maximum energy densities from sequence G in $10^{15}\ \mathrm{g/cm^3}$ units.

What has been illustrated in Fig. 7 for one sequence can be succinctly presented in the sequence plots (see Figs. 8–10), given that the focus of this study is the stability of these models. These figures show the gravitational mass vs the maximum energy density of constant angular momentum sequences.

First, we reproduce the finding of Weih *et al.* for a monotonic rotation law for a small sample of cases. The left panel of Fig. 8 shows the sequences for CE1 equation of

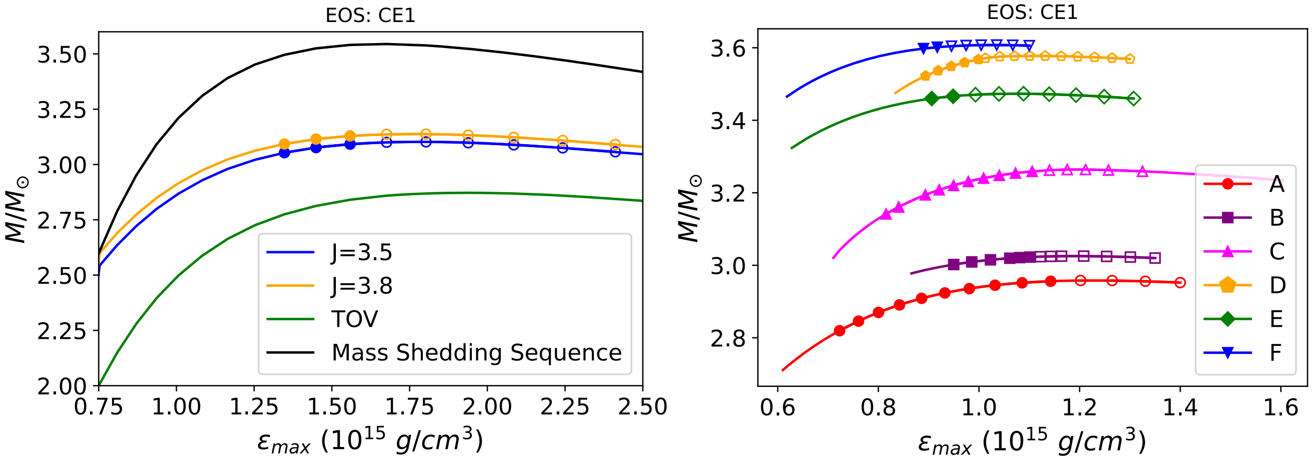

FIG. 8. Constant angular momentum sequences for CE1 entropy profile. The filled and empty shapes represent the stable and unstable configurations, respectively. *Left*: Sequences with j-constant rotation law [Eq. (1)]. Apart from j-sequences the TOV and mass-shedding sequence are shown. *Right*: sequences with Uryū rotation law [Eq. (8)].

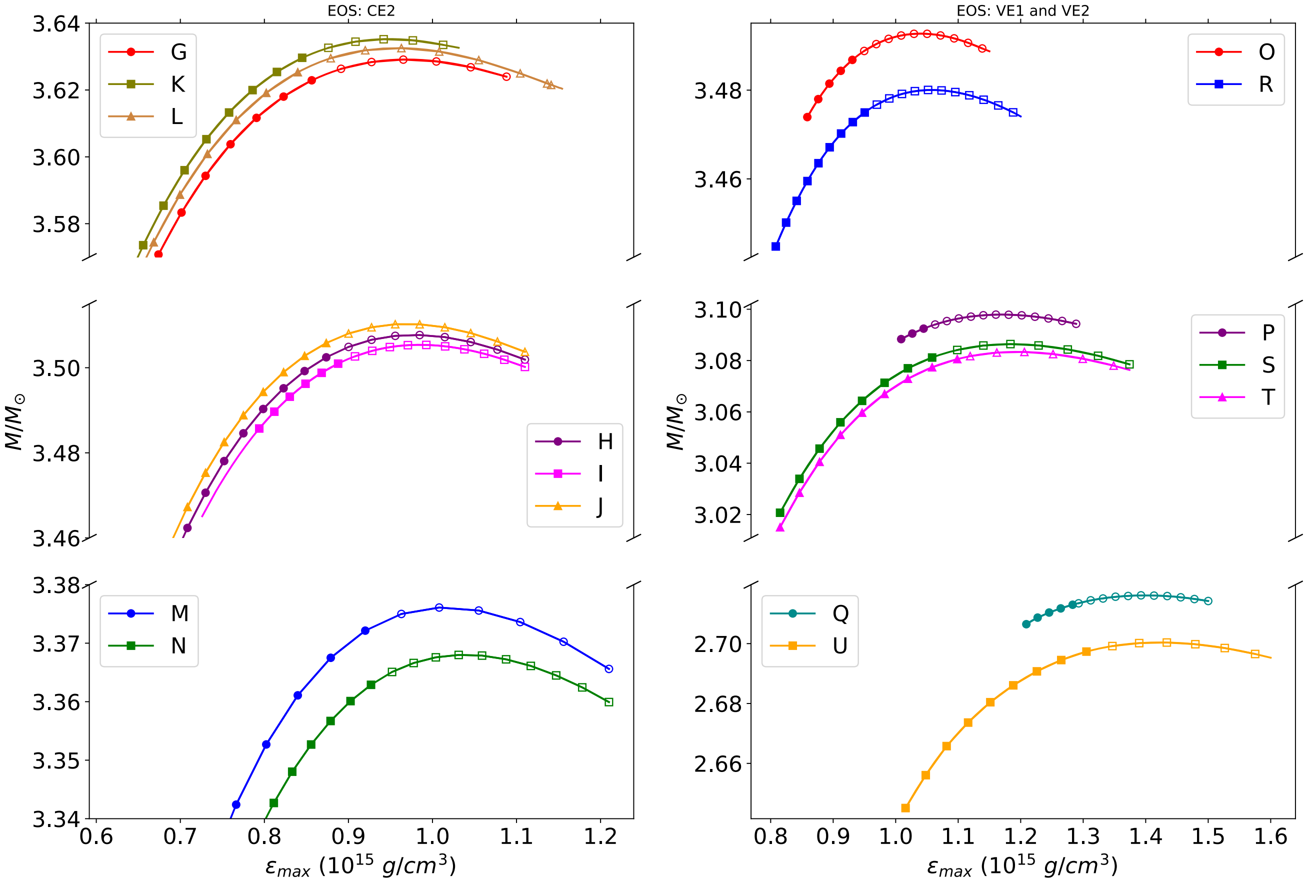

FIG. 9. Constant angular momentum sequences for Uryū rotation law. *Left*: Sequences with CE2 entropy profiles; *Right*: Sequences with variable entropy profiles (VE1 and VE2).

state for j-constant rotation law. The top and the bottom curves represent the mass shedding and the TOV sequences, respectively. The middle curves represent $J = 3.5$ and $J = 3.8$ sequences with a rotation parameter $A = 0.2$. The filled and unfilled markers on all the sequence figures represent the stars that were evolved on that respective sequence. The filled shapes represent the stars that were stable after the evolution and the hollow ones represent the stars that collapsed into a black hole (the density blew up) within the dynamical timescale. We find that the sequences with j-constant law follow the turning point criterion. All the stable stars lie on the low density side of the turning point. This result is consistent with the findings of Weih *et al.* [13].

In the right panel of Fig. 8 the constant angular momentum sequences with the Uryū *et al.* rotation law for the CE1 EOS cut are presented. The angular momenta of the sequences are 6, 6.5, 8.5, 10, and 11 (see Table I). All the stable stars lie on the left of the turning point. Furthermore, the transition from stable to unstable stars is close (within $\sim 0.2 \times 10^{15}$ $\mathrm{g/cm^3}$) to the turning point, consistent with the approximate turning point conjecture of Kaplan *et al.* [19].

In Fig. 9, different panels show sequences with different 1D cuts of the 3D DD2 equation of states. We note that because these sequences have constant $s(\rho)$, they do not have constant total entropy or total entropy per baryon. As $\rho_{\max}$ increases along a sequence, more of the low-entropy high-density region is sampled, and the specific entropy averaged over the star decreases. The panel on the left shows sequences of equation of state cut CE2. The panel on the right shows sequences with equation of state of variable entropy VE1 and VE2. The panels have been divided according to angular momentum ranges and EOSs for better visualization. Each of the sequences are constructed with different angular momenta and different combinations of A and B (see Table I). The A and B combinations are chosen to make neutron star mergerlike profiles. It is reflected in Fig. 6, where the rotation profile of a star on sequence G is plotted. The rotation profiles, in particular the $\Omega_{\max}/\Omega_c$ and the $\Omega_{\mathrm{eq}}/\Omega_c$, of the stars are similar to that of a neutron star merger remnant. It should be noted here that the maximum mass of the TOV sequences for all the EOS cuts and Uryū rotation law lies in the range $2.42M_\odot$–$2.44M_\odot$. Therefore, all the sequences here have maximum mass 20%–50% higher than the TOV mass indicating the stars on these sequences are hypermassive. The stability of stars on these sequences also conform to the approximate turning point conjecture.

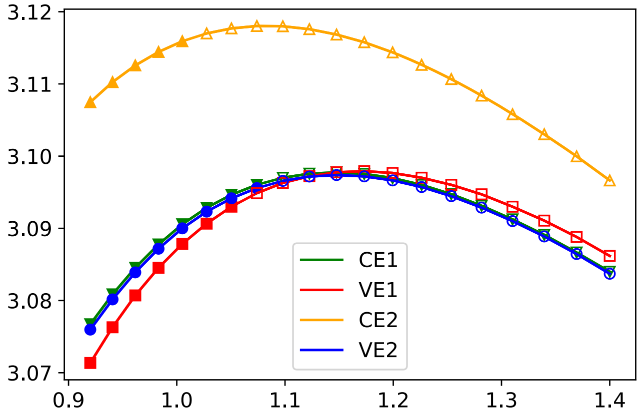

FIG. 10. Constant angular momentum sequences with the same angular momentum ($J = 7$), same A ($A = 0.65$) and B ($B = 0.45$) parameters but different entropy profiles.

In Fig. 10 we exhibit the effects of different entropy profiles on the turning point theorem. In order to do so, we show four sequences, all of them having angular momentum $J = 7$, Uryū rotation law parameters $A = 0.65$ and $B = 0.45$ and vary the entropy profiles only. All the sequences in this figure also satisfy the approximate turning point criterion. The equilibrium sequences themselves do not change greatly between one of the entropy profiles studied and another, which is not surprising given that the central region is degenerate in all cases. However, the mode determining radial stability extends into the nondegenerate region, so these simulations were needed to check the effect of entropy on dynamical stability.

Constant angular momentum sequences with constant A and B are not the unique way to construct sequences with this 2-parameter rotation law. This points to a certain ambiguity of application in the turning point criterion. Suppose a star belongs to two sequences of the same J but with different rotation profile parameter held fixed. Could the star be on the stable branch of one and the unstable branch of the other? We have therefore also evolved several constant J sequences with constant $\Omega_{\mathrm{max}}/\Omega_{\mathrm{c}}$ and $\Omega_{\mathrm{eq}}/\Omega_c$ (see Fig. 11 and Table II). The M vs ρ_{max} plots for these sequences are very close to the sequences of constant A and B with which they share a common starting point, so naturally the approximate turning point method works equally well for them. This is consistent with the assumption that M does not depend on angular momentum distribution to first order.

B. Dependence of M_{max} on A and B

It is already evident from the constant J sequence plots that the maximum mass does not vary greatly (~0.4%) with A and B parameters of the Uryū law as compared with its variation along angular momentum or the EOS cuts. This is consistent with the assumption of Kaplan *et al.* that M_{max} depends to first order only on the total angular momentum (and other global conserved quantities) and not its distribution.

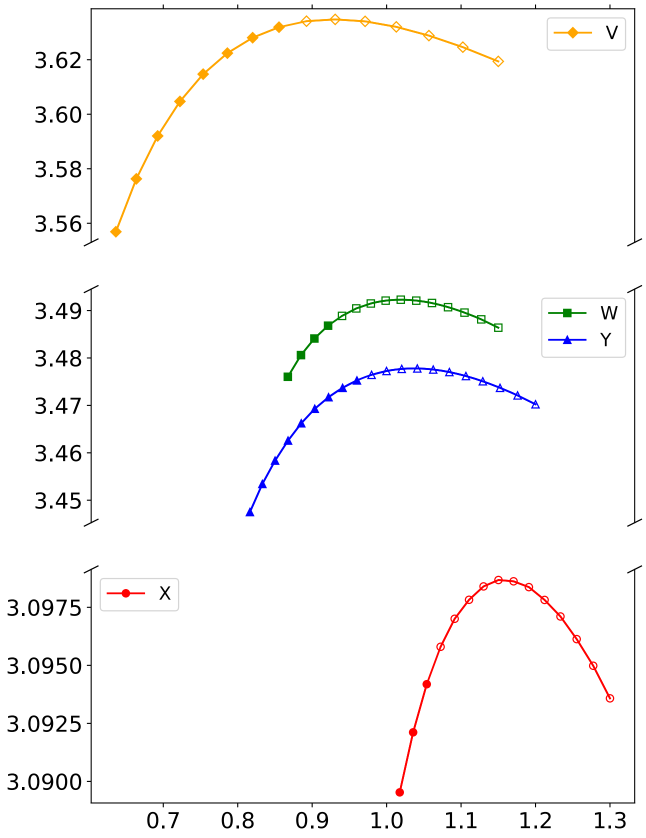

FIG. 11. Constant angular momentum and constant angular velocity sequences (see Table II).

Nevertheless, it is interesting to consider, for a flexible rotation law family like the Uryū law, what angular momentum distribution gives the largest increase in M_{max} for a given J. For this form of rotation law and a given equation of state, one can consider M_{max} a function of J, A, and B; $M_{\mathrm{max}}(J; A, B)$. For $J = 0$, we must recover the TOV limit for any A and B; $M_{\mathrm{max}}(0; A, B) = M_{\mathrm{TOV\ max}}$. Except for extremely high J, the effect of rotation can be well-approximated by the lowest-order quadratic [51] correction,

TABLE II. List of constant-J and constant angular velocity ratio sequences. From left to right, the columns represent the entropy profiles, angular momenta, ratio of maximum angular velocity to the central angular velocity, ratio of equatorial angular velocity to the central angular velocity, and sequence names, respectively.

EOS	J	$\Omega_{\mathrm{max}}/\Omega_c$	Ω_{eq}/Ω_c	Name
CE2	11	1.4	0.7	V
VE1	10	2.0	0.3	W
	7	2.0	0.3	X
VE2	10	2.0	0.5	Y

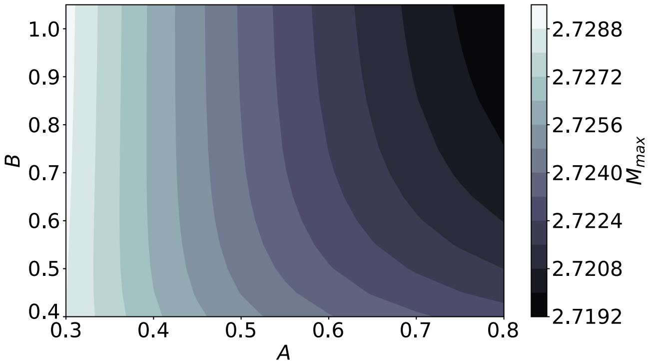

FIG. 12. Maximum mass for $J = 4$ sequences as a function of Uryū law rotation parameters A and B.

$$M_{\rm max}(J;A,B) \approx M_{\rm TOV\ max} + \left(\frac{dM_{\rm max}}{d(J^2)}\right)(A,B)J^2. \tag{17}$$

We can estimate this derivative $dM_{\rm max}/d(J^2)$ as a function of A and B by calculating the maximum mass for a modest J but a wide range of A and B. To this end, we have systematically explored the dependence of the maximum mass for entropy profile CE2 on A and B for one fixed J. Figure 12 illustrates the maximum mass of the sequences with $J = 4$ in the parameter space of A and B parameters of the Uryū rotation law. Note that this J is lower than that of most of the hypermassive sequences studied above. The plot shows not what is the greatest $M_{\rm max}$ attainable at any J, but which distribution of angular momentum gives the greatest enhancement of maximum mass for a given modest total angular momentum. In this plot the parameter A has been varied with an increment of 0.05, starting from 0.3 varying up to 0.8. The increment in B is the same with a range 0.4–1.05. We find that the maximum mass is more sensitive to A as compared to B in this range. This indicates greater sensitivity to the form of the rotation law at high j (farther from the axis) rather than at low j (closer to the axis). One might have expected the opposite, presuming that rotational support in the inner region would be most helpful in resisting gravitational collapse. However, for these realistic, nonmonotonic rotation profiles, rotation support is fairly unimportant in the core but crucial in the envelope [22]. Highest $M_{\rm max}$ for a given J is obtained for low A.

V. SUMMARY AND CONCLUSIONS

We have seen that the approximate turning point method successfully predicts stability for the range of entropy and nonmonotonic rotation profiles studied, chosen to model postmerger equilibria more realistically than previously realized. No doubt it would be possible to devise rotation and entropy profiles that resemble postmerger remnants even more closely. However, if the goal is to test turning point methods in extreme conditions under which they might fail, perhaps a better strategy would be to investigate less realistic profiles. For example, significantly wider exploration of entropy effects will confront the inconvenience that entropies high enough for a nondegenerate core will (assuming one insists on convectively stable $ds/d\rho < 0$ profiles) have thermally supported envelopes with extended low density region. This can, in fact, make the mass-shedding limit more severe [19].

In the process of carrying out this exploration of rotation law parameter space for hypermassive neutron stars with Uryū *et al.* equilibria, we have shown that we can generalize the RotNS code to cover a fair approximation to the realistic range of postmerger remnant rotation and entropy profiles. Investigations of the late-time (∼ seconds) evolution of binary neutron star and black hole-neutron star mergers often resort to 2D axisymmetric simulations. The initial data for these simulations has been either simple equilibria (e.g., constant entropy, j-constant rotation), which are artificial, or azimuthally averaged profiles of 3D mergers, and this averaging is a strong and sudden perturbation of the 3D system (even many that are "roughly axisymmetric") and can produce worrying transients. Axisymmetric equilibria with profiles extracted from merger simulations [e.g., a fit to A, B, and $s(\rho)$] might provide an attractive combination of the best of these two methods; arguably capturing as much realism from 3D merger profiles as 2D can accommodate while avoiding transients.

ACKNOWLEDGMENTS

M. D. gratefully acknowledges support from the NSF through Grant No. PHY-2110287 and through REU Grant No. PHY-2050886. M. D. and F. F. gratefully acknowledge support from NASA through Grant No. 80NSSC22K0719. F. F. gratefully acknowledge support from the Department of Energy, Office of Science, Office of Nuclear Physics, under Contract No. DE-AC02-05CH11231 and from the NSF through Grant No. AST-2107932. M. S. acknowledges funding from the Sherman Fairchild Foundation and by NSF Grants No. PHY-1708212, No. PHY-1708213, and No. OAC-1931266 at Caltech. L. K. acknowledges funding from the Sherman Fairchild Foundation and by NSF Grants No. PHY-1912081, No. PHY-2207342, and No. OAC-1931280 at Cornell. Computations for this manuscript were performed on the Wheeler cluster at Caltech, supported by the Sherman Fairchild Foundation. P. C.-K. C. acknowledge support from NSF Grant No. PHY-2020275 (Network for Neutrinos, Nuclear Astrophysics, and Symmetries (N3AS)).

[1] B. P. Abbott *et al.* (LIGO Scientific and Virgo Collaborations), GW170817: Observation of gravitational waves from a binary neutron star inspiral, Phys. Rev. Lett. **119**, 161101 (2017).

[2] B. P. Abbott *et al.* (LIGO Scientific and Virgo Collaborations), GW190425: Observation of a compact binary coalescence with total mass $\sim 3.4 M_\odot$, Astrophys. J. Lett. **892**, L3 (2020).

[3] B. P. Abbott *et al.* (LIGO Scientific, Virgo, Fermi GBM, INTEGRAL, IceCube, AstroSat Cadmium Zinc Telluride Imager Team, IPN, Insight-Hxmt, ANTARES, Swift, AGILE Team, 1M2H Team, Dark Energy Camera GW-EM, DES, DLT40, GRAWITA, Fermi-LAT, ATCA, ASKAP, Las Cumbres Observatory Group, OzGrav, DWF (Deeper Wider Faster Program), AST3, CAASTRO, VINROUGE, MASTER, J-GEM, GROWTH, JAGWAR, CaltechNRAO, TTU-NRAO, NuSTAR, Pan-STARRS, MAXI Team, TZAC Consortium, KU, Nordic Optical Telescope, ePESSTO, GROND, Texas Tech University, SALT Group, TOROS, BOOTES, MWA, CALET, IKI-GW Follow-up, H.E.S.S., LOFAR, LWA, HAWC, Pierre Auger, ALMA, Euro VLBI Team, Pi of Sky, Chandra Team at McGill University, DFN, ATLAS Telescopes, High Time Resolution Universe Survey, RIMAS, RATIR, SKA South Africa/MeerKAT Collaborations), Multi-messenger observations of a binary neutron star merger, Astrophys. J. Lett. **848**, L12 (2017).

[4] J. A. Faber and F. A. Rasio, Binary neutron star mergers, Living Rev. Relativity **15**, 8 (2012).

[5] L. Baiotti and L. Rezzolla, Binary neutron star mergers: A review of Einstein's richest laboratory, Rep. Prog. Phys. **80**, 096901 (2017).

[6] E. Burns, Neutron star mergers and how to study them, Living Rev. Relativity **23**, 4 (2020).

[7] J. M. T. Thompson, Stability predictions through a succession of folds, Phil. Trans. R. Soc. A **292**, 1 (1979).

[8] J. Katz, On the number of unstable modes of an equilibrium, Mon. Not. R. Astron. Soc. **183**, 765 (1978).

[9] J. Katz, On the number of unstable modes of an equilibrium–ii, Mon. Not. R. Astron. Soc. **189**, 817 (1979).

[10] R. Sorkin, A criterion for the onset of instability at a turning point, Astrophys. J. **249**, 254 (1981).

[11] R. D. Sorkin, A stability criterion for many parameter equilibrium families, Astrophys. J. **257**, 847 (1982).

[12] J. L. Friedman, J. R. Ipser, and R. D. Sorkin, Turning point method for axisymmetric stability of rotating relativistic stars, Astrophys. J. **325**, 722 (1988).

[13] L. R. Weih, E. R. Most, and L. Rezzolla, On the stability and maximum mass of differentially rotating relativistic stars, Mon. Not. R. Astron. Soc. **473**, L126 (2018).

[14] G. Bozzola, N. Stergioulas, and A. Bauswein, Universal relations for differentially rotating relativistic stars at the threshold to collapse, Mon. Not. R. Astron. Soc. **474**, 3557 (2018).

[15] E. Zhou, A. Tsokaros, K. Uryu, R. Xu, and M. Shibata, Differentially rotating strange star in general relativity, Phys. Rev. D **100**, 043015 (2019).

[16] P. L. Espino, V. Paschalidis, T. W. Baumgarte, and S. L. Shapiro, Dynamical stability of quasitoroidal differentially rotating neutron stars, Phys. Rev. D **100**, 043014 (2019).

[17] K. Takami, L. Rezzolla, and S. Yoshida, A quasi-radial stability criterion for rotating relativistic stars, Mon. Not. R. Astron. Soc. **416**, L1 (2011).

[18] M. Shibata, T. W. Baumgarte, and S. L. Shapiro, Stability and collapse of rapidly rotating, supramassive neutron stars: 3-D simulations in general relativity, Phys. Rev. **D61**, 044012 (2000).

[19] J. D. Kaplan, C. D. Ott, E. P. O'Connor, K. Kiuchi, L. Roberts, and M. Duez, The influence of thermal pressure on equilibrium models of hypermassive neutron star merger remnants, Astrophys. J. **790**, 19 (2014).

[20] F. Galeazzi, S. Yoshida, and Y. Eriguchi, Differentially-rotating neutron star models with a parametrized rotation profile, Astron. Astrophys. **541**, A156 (2012).

[21] Y. Eriguchi and E. Müller, A general computational method for obtaining equilibria of self-gravitating and rotating gases, Astron. Astrophys. **146**, 260 (1985), https://ui.adsabs.harvard.edu/abs/1985A%26A...146..260E/abstract.

[22] W. Kastaun and F. Galeazzi, Properties of hypermassive neutron stars formed in mergers of spinning binaries, Phys. Rev. D **91**, 064027 (2015).

[23] M. Hanauske, K. Takami, L. Bovard, L. Rezzolla, J. A. Font, F. Galeazzi, and H. Stöcker, Rotational properties of hypermassive neutron stars from binary mergers, Phys. Rev. D **96**, 043004 (2017).

[24] R. De Pietri, A. Feo, J. A. Font, F. Löffler, M. Pasquali, and N. Stergioulas, Numerical-relativity simulations of long-lived remnants of binary neutron star mergers, Phys. Rev. D **101**, 064052 (2020).

[25] P. Iosif and N. Stergioulas, Equilibrium sequences of differentially rotating stars with post-merger-like rotational profiles, Mon. Not. R. Astron. Soc. **503**, 850 (2021).

[26] P. Iosif and N. Stergioulas, Models of binary neutron star remnants with tabulated equations of state, Mon. Not. R. Astron. Soc. **510**, 2948 (2022).

[27] M. Cassing and L. Rezzolla, Realistic models of general-relativistic differentially rotating stars, Mon. Not. R. Astron. Soc. **532**, 945 (2024).

[28] K. V. Staykov, D. D. Doneva, L. Heisenberg, N. Stergioulas, and S. S. Yazadjiev, Differentially rotating scalarized neutron stars with realistic postmerger profiles, Phys. Rev. D **108**, 024058 (2023).

[29] K. Uryu, A. Tsokaros, L. Baiotti, F. Galeazzi, K. Taniguchi, and S. Yoshida, Modeling differential rotations of compact stars in equilibriums, Phys. Rev. D **96**, 103011 (2017).

[30] S. Typel, G. Röpke, T. Klähn, D. Blaschke, and H. H. Wolter, Composition and thermodynamics of nuclear matter with light clusters, Phys. Rev. C **81**, 015803 (2010).

[31] E. O'Connor and C. D. Ott, A new open-source code for spherically-symmetric stellar collapse to neutron stars and black holes, Classical Quantum Gravity **27**, 114103 (2010).

[32] https://stellarcollapse.org.

[33] A. Perego, S. Bernuzzi, and D. Radice, Thermodynamics conditions of matter in neutron star mergers, Eur. Phys. J. A **55**, 124 (2019).

[34] E. V. Shuryak, Quantum chromodynamics and the theory of superdense matter, Phys. Rep. **61**, 71 (1980).

[35] A. Bauswein, N.-U. F. Bastian, D. B. Blaschke, K. Chatziioannou, J. A. Clark, T. Fischer, and M. Oertel, Identifying a first-order phase transition in neutron star

mergers through gravitational waves, Phys. Rev. Lett. **122**, 061102 (2019).

[36] E. R. Most, L. J. Papenfort, V. Dexheimer, M. Hanauske, S. Schramm, H. Stöcker, and L. Rezzolla, Signatures of quark-hadron phase transitions in general-relativistic neutron-star mergers, Phys. Rev. Lett. **122**, 061101 (2019).

[37] L. R. Weih, M. Hanauske, and L. Rezzolla, Postmerger gravitational-wave signatures of phase transitions in binary mergers, Phys. Rev. Lett. **124**, 171103 (2020).

[38] A. Prakash, D. Radice, D. Logoteta, A. Perego, V. Nedora, I. Bombaci, R. Kashyap, S. Bernuzzi, and A. Endrizzi, Signatures of deconfined quark phases in binary neutron star mergers, Phys. Rev. D **104**, 083029 (2021).

[39] G. B. Cook, S. L. Shapiro, and S. A. Teukolsky, Spin-up of a rapidly rotating star by angular momentum loss: Effects of general relativity, Astrophys. J. **398**, 203 (1992).

[40] G. B. Cook, S. L. Shapiro, and S. A. Teukolsky, Rapidly rotating polytropes in general relativity, Astrophys. J. **422**, 227 (1994).

[41] K. Uryū, S. Yoshida, E. Gourgoulhon, C. Markakis, K. Fujisawa, A. Tsokaros, K. Taniguchi, and Y. Eriguchi, New code for equilibriums and quasiequilibrium initial data of compact objects. IV. Rotating relativistic stars with mixed poloidal and toroidal magnetic fields, Phys. Rev. D **100**, 123019 (2019).

[42] G. Camelio, T. Dietrich, M. Marques, and S. Rosswog, Rotating neutron stars with nonbarotropic thermal profile, Phys. Rev. D **100**, 123001 (2019).

[43] SpEC: Spectral Einstein code, https://www.black-holes.org/code/SpEC.html (Accessed Feb. 27, 2024).

[44] J. Jesse, M. D. Duez, F. Foucart, M. Haddadi, A. L. Knight, C. L. Cadenhead, F. Hebert, L. E. Kidder, H. P. Pfeiffer, and M. A. Scheel, Axisymmetric hydrodynamics in numerical relativity using a multipatch method, Classical Quantum Gravity **37**, 235010 (2020).

[45] F. Pretorius, Numerical relativity using a generalized harmonic decomposition, Classical Quantum Gravity **22**, 425 (2005).

[46] D. Hilditch, A. Weyhausen, and B. Brügmann, Pseudospectral method for gravitational wave collapse, Phys. Rev. D **93**, 063006 (2016).

[47] T. Matsushima and P. S. Marcus, A spectral method for polar coordinates, J. Comput. Phys. **120**, 365 (1995).

[48] B. Szilágyi, J. Blackman, A. Buonanno, A. Taracchini, H. P. Pfeiffer, M. A. Scheel, T. Chu, L. E. Kidder, and Y. Pan, Approaching the post-Newtonian regime with numerical relativity: A compact-object binary simulation spanning 350 gravitational-wave cycles, Phys. Rev. Lett. **115**, 031102 (2015).

[49] L. T. Buchman, M. D. Duez, M. Morales, M. A. Scheel, T. M. Kostersitz, and A. M. Evans, Numerical relativity multimodal waveforms using absorbing boundary conditions, Classical Quantum Gravity **41**, 175011 (2024).

[50] P. C.-K. Cheong, N. Muhammed, P. Chawhan, M. D. Duez, and F. Foucart, High angular momentum hot differentially rotating equilibrium star evolutions in conformally flat spacetime, Phys. Rev. D **110**, 043015 (2024).

[51] S. L. Shapiro and S. A. Teukolsky, *Black Holes, White Dwarfs, and Neutron Stars: The Physics of Compact Objects* (Wiley, 1986).